OPTIMIZED SKID-LANDING-GEARS FOR TWIN-ENGINE-LIGHT UTILITY HELICOPTER

Moritz Grawunder, Roman Reß, Christian Breitsamter
moritz.grawunder@aer.mw.tum.de
Institute of Aerodynamics and Fluid Mechanics
Technische Universität München

Abstract

The reduction of emissions in air transport is clearly a main goal of the aeronautical industry today, addressing both fixed wing aircraft and rotorcraft. The second phase of the ADHeRo (Aerodynamic Design Optimization of a Helicopter Fuselage including a Rotating Rotor Head) project contributed to achieving this goal by providing detailed flow characteristics and drag analysis of a state-of-the-art Twin Engine Light class utility helicopter with faired skid-landing-gears. This was achieved by means of wind tunnel experiments and numerical simulations. It has been shown that optimizing the aerodynamic design of the skid-landing-gear is a vital approach for achieving efficiency gains in the twin-engine-light helicopter class. Improving the aerodynamic design is obtained by fairing the circular cross-beams and attaching elements to the fuselage with streamlined panels. Furthermore, the fuselage bottom is smoothed. Two types of fairings were investigated - one retrofittable design for current production machines and a more progressive design for next generation helicopter. The analysis revealed that reducing the form and interference drag of the faired skid-landing-gear yields significant drag reductions. Compared to the baseline model, which excludes the tail surfaces, the parasite drag is reduced by 24 % and 27 % with the retrofittable and progressive landing-gear design, respectively.

SYMBOLS

A_{ref}	Reference area	[m^2]
C_D,C_L	Drag and lift coefficient	[-]
F_D,F_L	Drag and lift	[N]
$l_{x,ref}$	Reference length in x-direction	[m]
U_∞	Freestream velocity	[m / s]
y^+	Dimensionless wall distance	[-]
α	Angle of attack	[deg]
β	Angle of side slip	[deg]
ρ	Fluid density	[kg / m^3]
ω_x	Axial vorticity	[1 / s]

ABBREVIATIONS

ADHeRo	Aerodynamic Design Optimisation of a Helicopter Fuselage Including a Rotating Rotor Head
GRC	Green Rotorcraft Consortium
SEL	Single-Engine Light
TEL	Twin Engine Light
W/T	Wind Tunnel
ECD	Eurocopter Deutschland GmbH
TUM-AER	Aerodynamics and Fluid Mechanics at the Technische Universität München
Stereo-PIV	Stereo Particle Image Velocimetry
HWA	Hot-Wire-Anemometry
URANS	Unsteady Reynolds Averaged Navier Stokes
SST	Shear Stress Transport
F0M0	Baseline fuselage and mast fairing
F1M0	Fuselage with smoothed cabin bottom and baseline mast fairing
L0	Baseline skid-landing-gear
L1	Retrofittable faired skid-landing-gear
L2	Progressive faired skid-landing-gear
R0	Rotor Head

1. INTRODUCTION

The presented work is conducted in the framework of the project ADHeRo (Aerodynamic Design Optimization of a Helicopter Fuselage including a Rotating Rotor Head). ADHeRo is a subproject of the Joint Undertaking CleanSky within the Green Rotorcraft Consortium (GRC).

Reducing emissions (CO2, NOX, Noise) is clearly one of the most challenging tasks of the aeronautical industry today. In order to contribute to achieve efficiency gains for rotorcraft, ADHeRo is aiming to reduce parasite drag for Twin Engine Light (TEL) - class utility helicopters in level flight. In the helicopter fleet from the year 2000, the TEL-class accounted for approximately 10% of the global flight hours performed by civil helicopters [1]. Thus improving the efficiency in the TEL-class can have a relevant impact on the ecological foot print of the global helicopter fleet. For this reason, a state-of-the-art TEL - class utility helicopter with a bearingless main rotor system is subject to the optimisation performed through ADHeRo, see Fig. 1.

Fig. 1. Investigated state-of-the-art TEL-class utility helicopter [1].

The optimisation is conducted by developing and investigating one baseline and several modified configurations by means of wind tunnel experiments and numerical simulations.

The authors showed [2] that reducing parasite drag is a viable approach for achieving efficiency gains. Thus components which contribute the most to parasite drag are improved. These components are the fuselage, the rotor head and the landing-gear. However, possible changes in the generated down force of the modified components has to be taken into account. Otherwise, the increase in required rotor power (to compensate the additional down force) could deteriorate the achieved efficiency gains. The sensitivity of the total power requirements to changes in down force is much smaller than to changes in drag though. The reason for this is that the rotor acts much more efficiently in generating vertical than horizontal thrust. Thus it is advisable performing a trade-off study before the final selection.

Skid-landing-gears are the basic solution for landing-gears in the single- and twin-engine-light (SEL and TEL) helicopter class. Keys [3] shows that skid-landing-gears provide drag levels approximately 40% below fixed wheeled-landing-gears. However, wheeled-landing-gears can be retracted. This improves drag coefficients significantly. According to Keys the additional weight and complexity of retractable wheeled-landing-gears begin to pay off beyond flight speeds of 145 knots. Current SEL and TEL class helicopter cruising speeds are exceeding this barrier. Still retracting wheeled-landing-gears are not feasible for this helicopter class, because the fuselage volume is limited. Applying retractable wheeled-landing-gears would result in an increase in fuselage frontal area, e.g. by sponsons. This increase in frontal area would thwart the associated reduction in drag coefficient. Therefore, reducing parasite drag levels in the SEL class is typically achieved by replacing or fairing the cylindrical tubes on skid-landing-gear, e.g. EC120, R44 or MD600. In the TEL class similar solutions are known for an executive transport version of the EC145 T1.

In this paper the achieved improvements of the aerodynamic design through the application of new faired skid-landing-gear variants are presented for the ADHeRo configuration. The aerodynamic characteristics are analysed by means of wind tunnel experiments and numerical simulations.

2. MODEL GEOMETRY AND CONFIGURATIONS

The real helicopter geometry, which is to be reproduced using the ADHeRo wind tunnel (W/T) model, represents a characteristic state-of-the-art TEL utility helicopter with a maximum take-off weight of 2.95 metric tons, see Fig. 1. It features a five-bladed bearingless rotor and a backdoor at the rear fuselage upsweep, which is typical for a utility helicopter.

Fig. 2. Baseline configurations of the ADHeRo wind tunnel model (F0M0L0R0).

Fig. 2 a) depicts the ADHeRo W/T model in its full configuration. The design of the W/T model is primarily driven by the requirement of drag force prediction due to flow separation at the fuselage, skid-landing-gear and rotor head. A detailed description of the W/T model design methodology is given in [2].

Fig. 3 depicts the design of the W/T model rotor head in detail. As for the other model components, the real helicopter geometry is precisely reproduced on all components exposed to the flow. The model rotor head allows for collective and cyclic pitch motion of the blade cuffs through the application of a fully functional swash blade. The swash blade attitude is fixed at a position that represents the trimmed attitude for the real helicopter configuration in cruising flight. The blade cuffs are truncated at the radial position of the first aerodynamic efficient blade section.

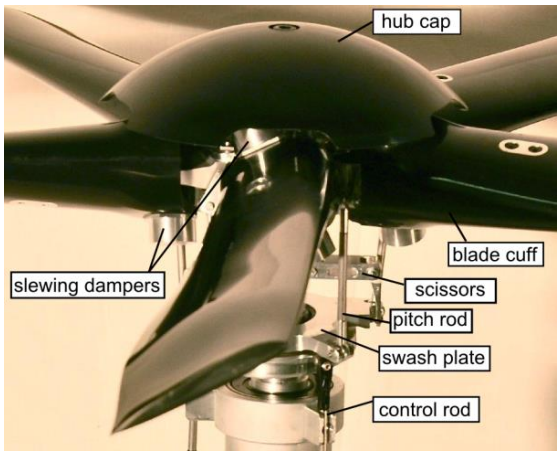

Fig. 3. Detail view of the model rotor head components.

2.1. Baseline Skid-Landing-Gear Variant

Fig. 4 depicts a detailed view of the baseline skid-landing-gear. The landing-gear design represents the typical design found on most helicopters without wheeled-landing-gears. It consists of the skids, the cross-beams and the long footsteps. Furthermore, the skid-landing-gear features blunt attaching elements to connect the different components and the entire landing-gear to the fuselage. The cross-beams are integrated into the fuselage through open cavities on the bottom of the fuselage. At the bottom of the fuselage further details are incorporated in the

baseline model, representing equipment attachment surfaces. The associated equipment is not modelled.

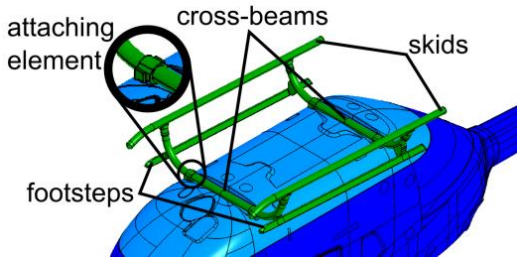

Fig. 4. Detail view of the baseline model skid-landing-gear components.

2.2. Modified Skid-Landing-Gear Variant L1

The general design philosophy for skid-landing-gear variant 1 (L1) is focused on the ability to retrofit the faired skid-landing-gear to current state-of-the-art SEL and TEL - class helicopters. The idea is to reduce the form and interference drag by fairing the circular cross-beams and attaching elements with more streamlined panels, see Fig. 5. The cross tube cover is obtained by fairing the front and rear cross tubes with panels featuring an airfoil cross section. This airfoil is of type DU-06-W200, developed by the TU Delft. chord. It provides a maximum thickness of 19.8% at 31.1% chord and a maximum camber of 0.5% at 84.6%. By extruding this profile at its thickness maximum along the centerline of the cross-beams, the fairing shape is obtained. The thickness of the airfoil section is scaled such that it encloses the cross-beam diameter with sufficient offset to the tube. An offset is necessary to comply with crash worthiness constraints. The twist at the junction between the fairing and the skids is set approximately to 0°. Towards the junction of the fairing with the fuselage, the twist is varied to a positive value. The impact on the static stability in pitch of the baseline fuselage is minimized by designing a fairing with a larger chord at the rear relative to the front cross tube. The L1-a1 design of the cross-beam covers is provided by the project leader Eurocopter Deutschland GmbH (ECD), see Fig. 5.

Based on this input several modifications to the first design were investigated in the Institute of Aerodynamics and Fluid Mechanics at the Technische Universität München (TUM-AER). An overview of the five variants of L1, which are developed at TUM-AER based on the input of ECD, are depicted in Fig. 5. The design variants can be subdivided into two categories. The variants “a” only deviate from the design provided through ECD in the geometry of the additional central cross-beam covers and the additional extensions downstream the attaching elements to the fuselage, where a1 is the actual input geometry. L1-a1 is the most basic type of fairing without the central cross-beam covers or extensions and L1-a3 is the most complex version with central cross-beam covers and extensions. Variant L1-a2 is of intermediate complexity with no additional extensions but with central cross-beam covers attached.

For variants “b” more changes to the original ECD design were incorporated. Especially, the fairing of the attachment elements of the skid-landing-gear and the fuselage is modified. The modifications aim at reducing the frontal area of this part of the fairing to reduce its form drag. Through preliminary numerical simulations it is found that the additional covers investigated on variants a2, a3, b2 and b3 don’t show the desired effect. The best variants (a3 and b3) only reproduce the drag savings of the two most basic variants (a1 and b1), but at the cost of an increased down force. Variant b1 is selected for W/T testing and more detailed numerical analysis. The reason for this is the simplicity of the shape and the highest drag savings observed of all variants.

.

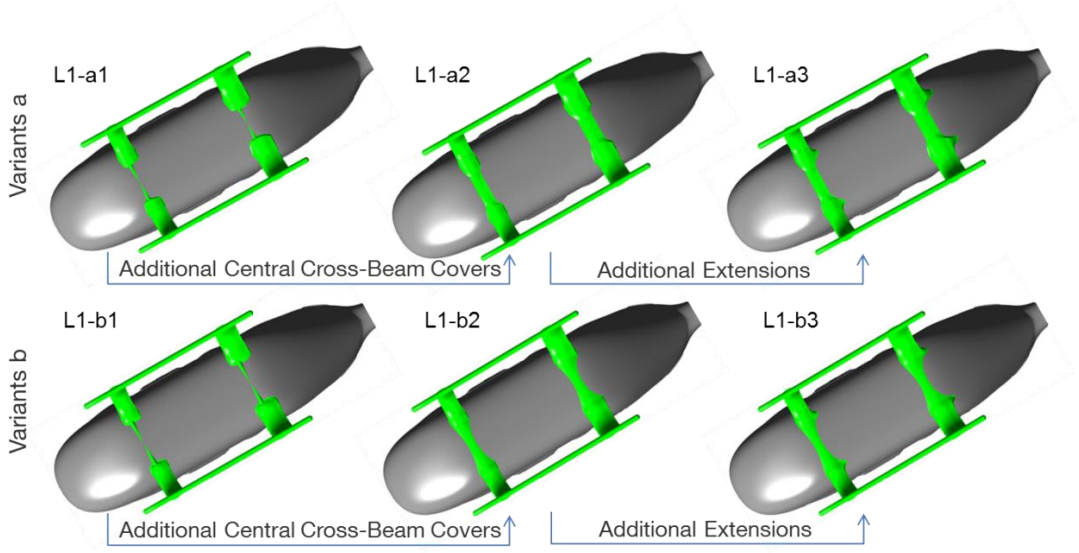

Fig. 5. Considered skid-landing-gear modifications for the design of skid-landing-gear modification L1.

The lowest drag value is obtained by designing the attachment elements such that the frontal area is minimized without violating functional constraints, see Fig. 6.

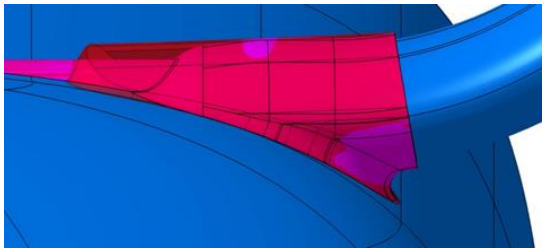

Fig. 6. Minimized frontal area of attaching element for variant L1-b1 compared to L1-a1 (translucent).

Furthermore, the bottom of the fuselage is smoothed by removing the attaching surfaces for additional equipment

2.3. Modified Skid-Landing-Gear Variant L2

The second modification of the skid-landing-gear L2 is a more progressive design. It is not retrofittable to current production models. The reason for this is the displacement of the cross-beam position vertically into the fuselage. Thus more profound structural changes to the fuselage would be necessary to realize this design. However, from an aerodynamic point of view this design provides advantages. The enhancement of this solution is that the flow past the bottom of the fuselage is no longer disturbed by the central cross-beam elements or fairings. This is expected to further postpone the separation at the rear fuselage upsweep. Hence, additional drag savings should be possible. Furthermore, displacing the cross-beams vertically leads to a reduced frontal area, which should also yield additional drag reductions.

Compared to the first variant L1, the cross-beam fairing is subjected to additional optimizations. Based on the fairing L1-a1 numerical simulations are performed by ECD for varying chord and twist distributions of the airfoil section along the cross-tube.

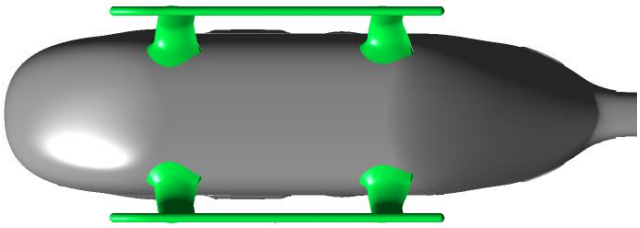

Fig. 7. Geometry of landing skid modification variant L2.

The optimization of the chord and twist distribution is varied independently for the front and rear cross-tubes over three different sections (inner, middle and outer). The design optimization is performed with the objective of decreasing the total drag level without increasing the down-force. At later stage flight mechanic consideration could be taken into account as well. ECD investigated a total of 21 different configurations numerically. The solution providing the best compromise between the two design objectives is selected for further analysis through TUM-AER, see Fig. 7.

3. WIND TUNNEL EXPERIMENTS

All W/T experiments conducted within ADHeRo are performed in W/T A at TUM-AER. W/T A is of closed return type and can be operated either in an open or closed test section configuration. For ADHeRo, the test section is always operated in an open configuration, allowing a maximum free stream velocity U_∞ of 65 m/s. The standard freestream velocity for the ADHeRo measurements is 40 m/s. This corresponds to a freestream Reynolds number Re_∞ of approximately $1 \cdot 10^6$. The freestream Mach number Ma_∞ is 0.1. For this paper, no variations in angle of attack α and angle of sideslip β are considered. All results shown in this paper are recorded at α, β = 0°. W/T A provides a freestream turbulence intensity below 0.4 % in all three directions in space.

3.1. Aerodynamic Force Measurements

The global aerodynamic forces and moments acting on the model are recorded with a six-component under-floor W/T balance. All recorded data are time-averaged. Preliminary testing revealed that the measured forces and moments become independent of the integration time for intervals of minimum 15 seconds. Thus this value is chosen for the aerodynamic force and moment measurements performed.

Component loads are measured through the installation of an internal six-component strain gauge balance. Through the application of this balance it is possible to derive a more detailed analysis of interference drag effects by recording component loads. In combination with the variation of measured configurations, i.e. with or without a certain component, a detailed drag breakdown can be obtained. Fig. 8 depicts the two different installations employed for measuring the rotor head and the skid-landing-gear loads.

In this paper, all of the force data presented are made dimensionless. The resulting aerodynamic coefficients for drag C_D and lift C_L are assessed through Eq. (1) and (2).

(1) $$C_D = \left(\frac{F_D}{\frac{1}{2}\rho \, {U_\infty}^2 \, A_{ref}} \right)$$

(2) $$C_L = \left(\frac{F_L}{\frac{1}{2}\rho \, {U_\infty}^2 \, A_{ref}} \right)$$

Note that the reference area A_{ref} is kept constant for all investigated configurations to facilitate the comparison of the respective aerodynamic coefficients.

a)

b)

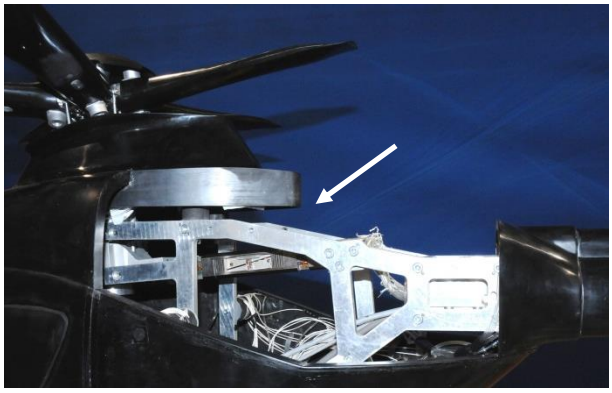

Fig. 8. Installation of a six-component strain gauge balance for measuring a) skid-landing-gear and b) rotor head loads.

3.2. Stereo Particle Image Velocimetry

Three-dimensional velocity field data is recorded in the wake of the W/T model through the application of Stereo Particle Image Velocimetry (Stereo-PIV). Conventional PIV can only provide two-dimensional velocity vectors within the measuring plane. The employed Stereo-PIV system allows recording the velocity components normal to the measuring plane by exploiting the principles of stereogrametry.

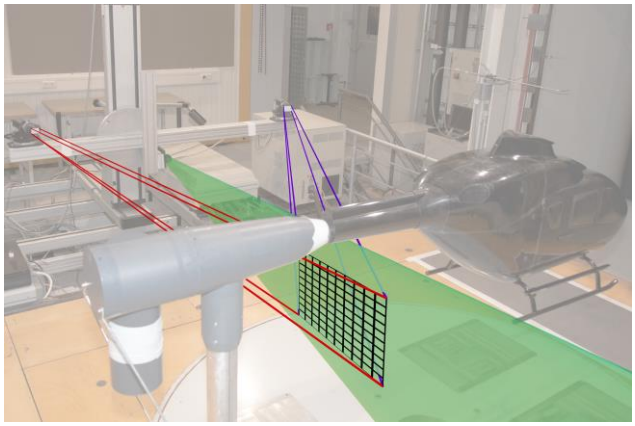

Fig. 9. Stereo PIV measurement setup.

The Stereo-PIV setup employed for ADHeRo is depicted in Fig. 9. For each measurement position 134 data samples are recorded at a sample rate of 10 Hz. The presented velocity data are averaged over all valid data samples. This typically results in an average over 100 data samples for the results presented herein.

(3) $$u_{rms} = \left(\frac{1}{n-1}\sum_{i=1}^{n}(u_i - \bar{u})^2\right)^{\frac{1}{2}}$$

Furthermore, the velocity fluctuations are extracted from the number n of all valid data samples i. The velocity fluctuations in the axial direction are given as root mean square (RMS) values, see equation (3).

3.3. Hot-Wire-Anemometry

In order to cross-check the statistical analysis of the Stereo-PIV data, hot-wire-anemometry (HWA) measurements are performed at selected positions.

Fig. 10. Constant temperature hot-wire-anemometry measurement setup and detailed view of the in-house designed triple-sensor-probe.

The advantage of HWA compared to Stereo-PIV measurements is the higher sample rate. Measurements presented in this paper are performed with an in-house designed triple-sensor-probe, see Fig. 10. The sample rate is set to 3000 Hz for all measurements. This corresponds to a total record of $45 \cdot 10^3$ samples due to the long measurement time of 15 s. Thus statistical quantities can be calculated accurately. The obtained data set is low-pass filtered at 1000 Hz. Based on this filtered data set the same statistical quantities as for the Stereo-PIV measurements are calculated, see equation (3).

4. NUMERICAL METHOD

In this section, the employed numerical method is described in detail. This includes the mesh generation process and the numerical setup for the different runs performed. Furthermore, the digital model geometry is presented and compared to the actual W/T model geometry.

4.1. Mesh Generation

The mesh generation is executed with the commercial meshing tool ANSYS ICEM CFD. The digital helicopter model is of the same scale as the physical W/T model. Concerning the level of geometrical details, the digital model is basically identical to the W/T model. Only the horizontal conus of the model support is incorporated in the digital model, while the other parts of the support are neglected. In analogy to the different configurations investigated through experiments, the flow is simulated for configurations F0M0L0R0, F1M0L2 and F1M0L2; see Fig. 11.

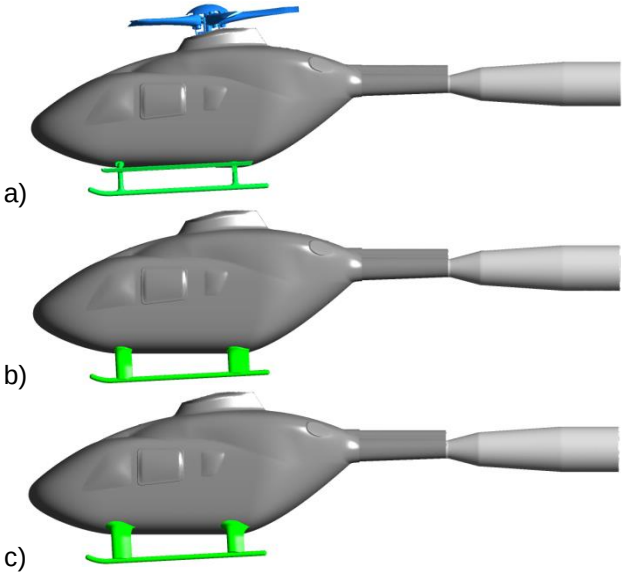

Fig. 11. Geometry used for numerical simulation of the W/T model flow, a) F0M0L0R0, b) F1M0L1 and c) F1M0L2.

However, the rotating rotor head including cyclic pitch is only incorporated for the baseline configuration to reduce the numerical effort.

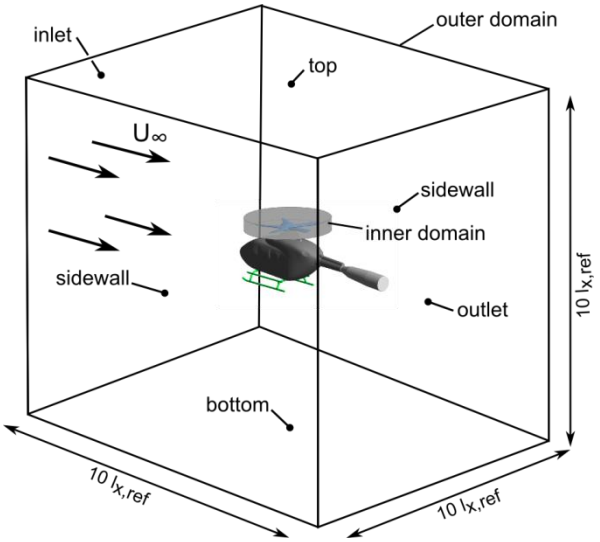

Fig. 12. Division of the computational domain into inner and outer domain including dimensions.

In [4] the authors present a detailed description how the rotation and cyclic pitch motion of the rotor head and blade cuffs is model through sliding meshes and deforming meshes, respectively. The outer domain covers the fuselage with skid-landing-gears and the far field; whereas the inner domain includes the rotor head, see fig. 12.

For the actual meshing of the investigated configurations, unstructured meshes are chosen. The meshing is performed by applying the Octree method first to obtain the surface grids. Before computing the volume mesh with the Delauney algorithm, the surface grids are subjected to several smoothing loops. The obtained volume mesh is again smoothed before adding the prism layers. The prism layers, consisting of 24 single layers, are generated near solid walls. Thereby the equivalent dimensionless wall distance y^+ is confined below one on all no-slip surfaces.

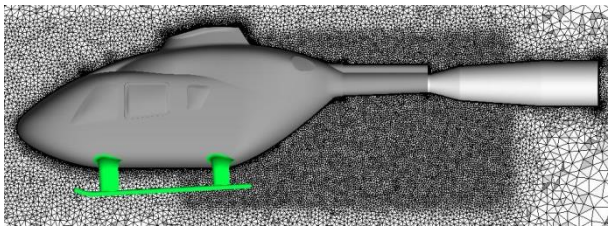

Fig. 13. Mesh topology in center plane near configuration F1M0L2.

The final mesh in the vicinity of the model is depicted in Fig. 13 for configuration F1M0L2. Note that the grid in the wake of the model is additionally refined in order to capture the flow topology in the wake more precisely.

4.2. Solver Setup

All numerical results presented in this paper are obtained by solving the incompressible Unsteady Reynolds Averaged Navier Stokes (URANS) equation. For this purpose, the commercial solver ANSYS CFX 5 is used. All runs are executed by employing the standard Shear Stress Transport (SST) turbulence model [5].
For the spatial discretization, a High Resolution Scheme is employed, blending between first and second-order accuracy. The temporal discretization is realized through the application of the implicit Backward – Euler – Method with second-order accuracy. All simulations are performed by employing a physical timescale of $1 \cdot 10^{-4}$ s. For details on the solver theory, please refer to [6].
The boundary conditions for the simulations are imposed by defining

- the inflow with a constant velocity profile (turbulence intensity of 5%) at the inlet,
- the outflow with zero pressure gradient at the outlet
- no-slip walls at the surface of the model and

- free-slip walls at the sidewalls, the top and the bottom of the domain.

The simulations are initialized by imposing the inlet conditions on the entire computational domain.

5. Results

First of all, the status quo in terms of drag is reviewed. Based on the analysis presented in [2] the drag breakdown for the baseline model is assessed. Through the application of the internal strain gauge balance, the drag breakdown is further detailed. Now, the component loads for the rotor head and the skid-landing-gear can be recorded separately. Thus it is possible to assess the magnitude of interference drag of these components too. Fig. 14 depicts the obtained detailed drag breakdown for configuration F0M0L0R0.

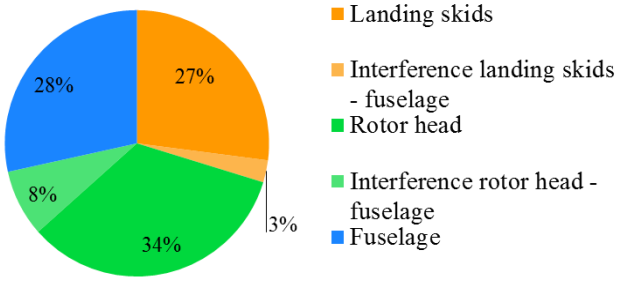

Fig. 14. Drag breakdown for the baseline W/T model configuration F0M0L0R0 (Re_∞ = 1.0 10^6, Ma_∞ = 0.116 , α = 0°, β = 0°).

The rotor head causes 42% of the parasite drag of configuration F0M0L0R0. This splits up into fractions of 34 % form drag and about 8 % interference drag on the fuselage. For the skid-landing-gear, different trends are observed. The fraction of the drag caused by the skid-landing-gear associated to interference effects is smaller. The gear causes 30 % of the total parasite drag, whereof only 3 % are associated to interference drag on the fuselage. Thus, fairing the circular tubes of the skid-landing-gear is a valuable approach for achieving drag reductions. Furthermore, the bluff adapter attaching the skid-landing-gear to the fuselage should also be faired. The positive effect of this measure is discussed at the end of this section.

Configuration	C_D [-]	$\Delta C_{D,\ F0M0L0R0}$ [%]
F0M0L0R0	0.302	-
F1M0L1R0	0.221	**- 26.8 %**
F1M0L2R0	0.212	**- 29.8 %**

Table 1. Comparison of drag coefficients for configurations F0M0L0R0, F1M0L1R0 and F1M0L2R0 (Re_∞ = 1.0 106, Ma_∞ = 0.116 , α = 0°, β = 0°).

Table 1 shows the absolute drag coefficient for the baseline configuration including the rotor head and skid-landing-gear. In addition, the drag coefficients of the configurations with the faired skid-landing-gears L1 and L2 are given. Furthermore, Table 1 states the relative difference in drag to the baseline configuration for configurations F1M0L1R0 and F1M0L2R0. Comparing the drag levels of the configurations with faired skid-landing-gears and smoothed cabin bottom against the baseline reveals a reduction of about one third. Thus, the applied fairings in combination with the smoothed cabin bottom prove highly effective for reducing parasite drag. The modified configuration with the progressive design variant L2 provides a slightly better drag reduction potential. However, the difference to the configuration with the retrofittable variant L1 amounts only to some 3 %. This indicates that the additional effort, which would be necessary for realizing L2, cannot solely be justified through drag benefits.

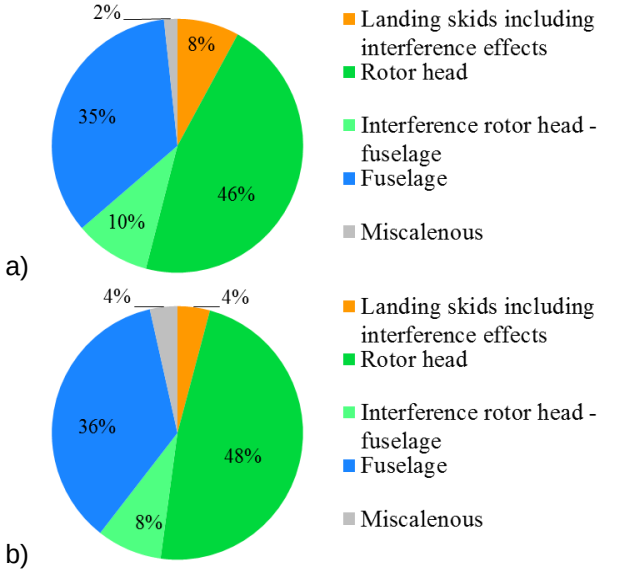

Fig. 15. Drag breakdown for the configurations with faired skid-landing gear a) L1 and b) L2. The drag components are given in percent of the baseline configuration (F0M0L0R0) to identify the obtained drag reduction (Re_∞ = 1.0 10^6, Ma_∞ = 0.116 , α = 0°, β = 0°).

Fehler! Verweisquelle konnte nicht gefunden werden. a) and b) show the changed drag breakdown when the faired skid-landing-gears L1 and L2 are attached on configurations F1M0L1R0 and F1M0L2R0, respectively. Unfortunately, the drag fraction due to interference effects of the gear on the fuselage cannot be assessed. The reason for this is the smooth surface transition between the faired gears and the fuselage. Thus the internal balance cannot be attached to the landing-gear without obstructing the measurements through additional fittings. However, it still becomes clear that the impact of the landing-gear, including interference effects on the fuselage, is significantly reduced. For the baseline configuration F0M0L0R0

this drag fraction aggregates to some 30 % of the total drag. By installing the faired skid-landing-gears, this drag fraction is reduced well below 10 %. For configuration F1M0L2R0 the drag fraction associated to the landing-gears is even confined to 4 %. This corresponds to a drag reduction associated to the landing-gear L1 and L2 form and interference drag of 24 % and 27 %, respectively. The other drag fractions are increased. However, this is mainly associated to the reduced reference drag level and not to a change in the component loads.

Calculating the absolute contribution to drag of the smoothed fuselage bottom reveals that this change accounts for the remaining difference in drag. Removing the flat attachment surfaces for additional equipment on the baseline fuselage returns another 3 % drag gain. Hence, whenever possible, such surfaces should only be considered for machines actually flying the associated equipment.

Configuration	$C_{L,\,total}$ [-]	$C_{L,\,LG}$ [-]	$C_{L,\,RH}$ [-]	$C_{L,\,FS}$ [-]
F0M0L0R0	0.046	0.074	0.052	-0.080
F1M0L1R0	-0.049	-0.001	0.054	-0.102
F1M0L2R0	-0.022	0.012	0.068	-0.102

Table 2. Comparison of the landing-gear (LG), rotor head (RH), fuselage (FS) and the total lift coefficients for configurations F0M0L0R0, F1M0L2R0 and F1M0L2R0 (Re_∞ = 1.0 10^6, Ma_∞ = 0.116 , $\alpha = 0°$, $\beta = 0°$).

Even more drastic changes, compared to the baseline, are observed for the occurring lift at the configuration with smoothed fuselage bottom and faired skid-landing-gears. For both the configuration F1M0L1R0 and F1M0L2R0 the modifications lead to a change of sign in the produced lift. For the baseline the total balance of vertical forces leads to a positive lift. Whereas, for the modified configurations a negative lift is observed. By differentiating between the configurations measured, the contribution to lift of each component is assessed. Changes due to interference effects with other components are not accredited separately. Table 2 shows the resulting total, landing-gear, rotor head and fuselage lift coefficients of the three investigated configurations. The first fact which becomes clear is that the origin of the down force is the fuselage. All other components successively add lift, except landing-gear L1 which basically does not contribute lift at all. The reason for the generation of down force at the fuselage is due to the rear upsweep featuring a negative “camber”. Thus as long as the flow remains attached, this generates down force. From table 2 it can be seen that the new smoothed fuselage bottom increases this effect. This results in a higher down force generated at the fuselage. Thus the effect of delayed separation through the smoothed cabin bottom is not only observed in drag, but in lift as well. For all three configurations the rotating rotor head generates lift. First of all the blade cuffs are optimized for low drag, resulting in a streamlined shape, see [7]. Thus on the rotating rotor head they generate lift in consequence of the collective and cyclic pitch input. Furthermore, a hub cap is installed, which generates additional lift through its positive camber. What seems surprising at first is that the baseline landing-gear generates lift. In previous publications [2,8] the authors showed that this added lift results from triggering an extension of the separation region on the rear-fuselage upsweep through the landing-gear. Hence, the deflection of the flow and in consequence the down force is reduced. The faired skid-landing-gear L2 also adds lift to the total balance. Compared to the baseline landing-gear the magnitude is significantly smaller. The probable reason for this is that the faired landing-gear is reducing interference drag on the fuselage. Hence, the resulting separation region on the rear fuselage upsweep is smaller. On the other hand, as described in section 2, the fairings of the landing-gears are designed to generate some lift through the applied twist variation. Obviously landing-gear L2 is generating more lift, or less down force on aggregate, than L1. The observed difference, in generated down force between L1 and L2, could provide reasoning for accepting the additional effort in realizing L2, since higher down forces could deteriorate efficiency gains, see section 1.

The impact of the observed drag reduction is also noticeable in the wake structure. Fig. 16. shows velocity fields in the wake of the three different configurations investigated before. The depicted contours of axial velocity deficit, compared to the freestream velocity U_∞, are obtained through Stereo-PIV measurements. The employed measurement setup is presented in section 3.2. In Fig. 16 a) a significant region of velocity deficit is recorded at one axial position in the wake of configuration F0M0L0R0. The axial position of the cut plane is indicated in the small box on the left.

The large extension of the region with decreased axial momentum correlates with the comparatively high form and interference drag of the baseline skid-landing-gear. In comparison to the baseline, the momentum losses associated to drag in the wake of the configurations with faired skid-landing-gears are significantly reduced. This is indicated by the drastically reduced velocity deficit in the wake of these configurations, depicted in Fig. 16 b) and c). The aerodynamic efficiency of the applied fairings becomes obvious by two features in the contours of axial velocity deficit. First of all the velocity deficit associated to the wake of the faired skid-landing-gears is barely observable. For the baseline landing-gear this wake is characterized by two distinct bulges of velocity deficits up two 40 % compared to the freestream.

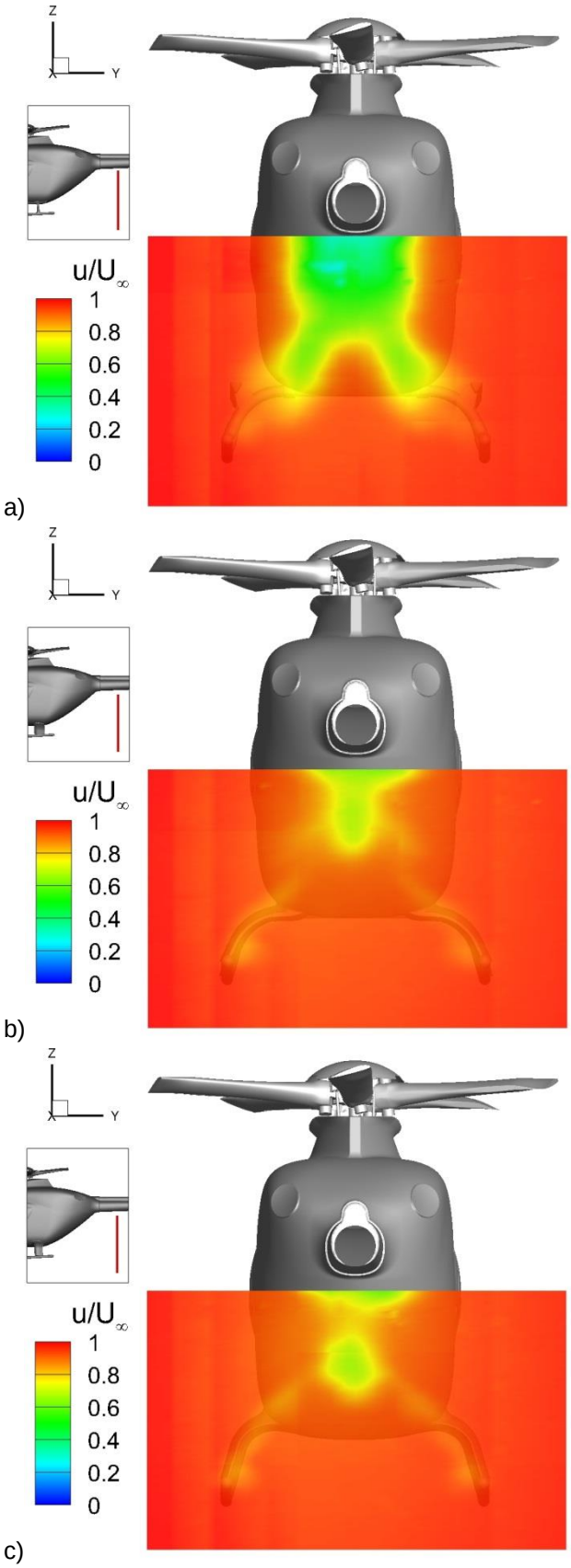

Fig. 16. Contours of axial velocity deficit in the wake of configuration F0M0L0R0, F1M0L1R0 and F1M0L2R0, obtained through Stereo – PIV (Re_∞ = 1.0 10^6, Ma_∞ = 0.116, α = 0°, β = 0°).

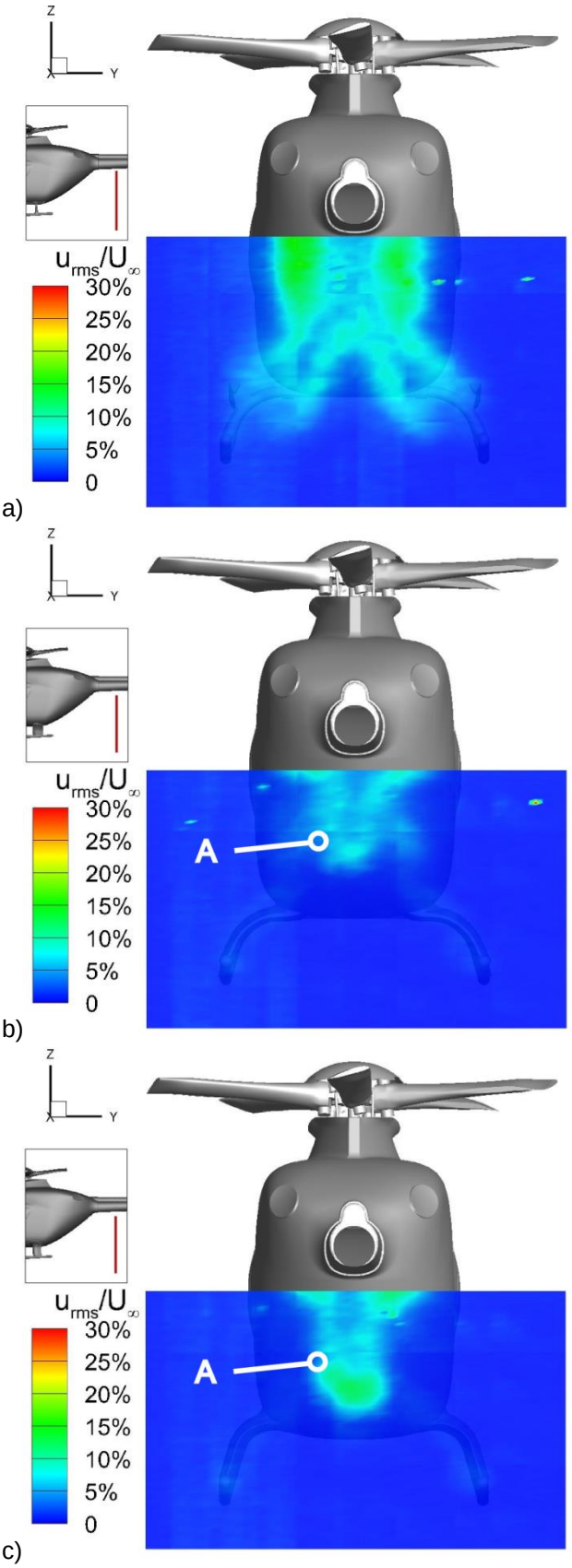

Fig. 17. Contours of RMS values of axial velocity fluctuations in the wake of configuration F0M0L0R0, F1M0L1R0 and F1M0L2R0, obtained through Stereo – PIV (Re_∞ = 1.0 10^6, Ma_∞ = 0.116 , α = 0°, β = 0°).

Downstream of the faired gears only a thin sheet of low velocity deficits around 10 % are recorded. Furthermore, the velocity deficit in the wake downstream of the fuselage itself is also reduced for configurations F1M0L1R0 and F1M0L2R0 compared to the baseline. This supports that fairing the attachment elements of the landing-gear also reduces the interference drag on the fuselage. Thereby, further evidence is also found for the origin of the observed change of sign in lift on the new configurations. Apparently this is mainly associated to delayed separation on the rear fuselage upsweep in the presence of the faired landing-gears.

In addition, the flow at the rear fuselage upsweep seems to be shifted from an eddy type to a vortex type of flow by attenuating separation on the rear fuselage upsweep, see [9]. In a vortex type of flow, as described by Seddon and Newman, strong vortices are formed on both sides of the fuselage. A more detailed analysis of this shift of the flow topology is presented at the end of this section. Unfortunately, these vortices are shed into the wake on each side of the tailboom. Thus they could not be detected through Stereo-PIV measurements. The reason for this is the obstruction of the Stereo-PIV cameras line of sight through light reflecting at the tailboom.

Finally, the velocity deficits in the wake of the configurations with faired skid-landing-gears are compared against each other. It can be observed, that the shape of the region of increased velocity deficits changes depending on which landing-gear is attached. In the wake behind configuration F1M0L2R0 an isolated spot of increased velocity deficit is observed. Whereas, behind the configuration with the retrofittable faired skid-landing-gear, F1M0L1R0, the fuselage wake is only contracted. In both cases the structures observed in the wake of the fuselage seem similar to those on the fuselage without any landing-gear attached, see [2]. Thus, the observed contraction is probably related to the formation of strong vortices on the side of the rear fuselage upsweep. As already mentioned, a more detailed study of this effect is presented in the analysis of the numerical simulations at the end of this section.

To supplement this analysis the Stereo-PIV results are post-processed to obtain root mean square (RMS) values of the axial velocity fluctuations u_{rms}, see section 3.2. Fig. 17 a), b) and c) show contours of u_{rms} referred to the freestream velocity U_∞ in a plane downstream of the lower aft-body of configurations F0M0L0R0, F1M0L1R0 and F1M0L2R0. In addition to the Stereo-PIV measurements the velocity fluctuations in the wake of the modified configurations are investigated by means of constant temperature hot wire anemometry (HWA) at selected points. First both the results obtained through HWA and Stereo-PIV are compared quantitatively to confirm the validity of both methods.

Configuration	u_{rms}/U_∞ (HWA)	u_{rms}/U_∞ (PIV)
F1M0L1R0	6.6 %	4.2 %
F1M0L2R0	6.9 %	4.6 %

Table 3: Comparison of RMS values of axial velocity fluctuations obtained through HWA and PIV for configuration F1M0L1R0 and F1M0L2R0 at position A (Re_∞ = 1.0 106, Ma_∞ = 0.116 , $\alpha = 0°$, $\beta = 0°$).

This is necessary since the statistical analysis of the Stereo-PIV results is based on a comparatively small set of data samples (maximum of 134 samples). Furthermore, the sample rate for the Stereo-PIV measurements is considerably smaller than for the HWA measurements (10 Hz compared to 3000 Hz). Table 3 presents the RMS value of the axial velocity fluctuations in percentage of the free stream velocity at position A, see Fig. 17 b) and b). The general trend that the fluctuations at position A for configuration F1M0L2R0 are increased compared to F1M0L1R0 is reproduced with both methods. However, the relative difference of the Stereo-PIV results to the HWA results is as high as 35%. Thus, to obtain quantitative results one should still rely on HWA results. The performed post-processing routine of the Stereo-PIV results is valid though to obtain qualitative information about the turbulent content in the wake. Hence, the main advantage of the method is that it provides a fast insight into the turbulent structures in the wake without perturbing the flow through probing equipment or hours of recording time for one measurement plane.

Characteristic for all contours of the axial velocity fluctuations is the increased level of fluctuations along the edge of the fuselage and landing-gear wake region. This is a result of the free shear layer shedding into the wake. The highest fluctuation level behind the lower aft-body is observed in the wake of the baseline configuration. Especially, on both side of the rear fuselage upsweep pronounced regions of increased fluctuations are revealed. They are related to the massive flow separation observed in the presence of the baseline skid-landing-gear. As shown at the end of this section this massive separation leads to an eddy type of flow at the rear-fuselage region. This probably results in the observed regions of higher fluctuations instead of two concentrated spots observed for a vortex type of flow.

Two differences in the axial velocity fluctuations are recorded between the baseline and the configurations with faired landing-gears. The first difference is that the two pronounced regions of fluctuations on each side of the fuselage, found downstream of the baseline configuration, are no longer detectable. This indicates a shift to a vortex

type of flow, were the separating shear layer is rolling up into two concentrated upsweep vortices. Unfortunately, as already mentioned, the region where these vortices pass the measurement plane could not be resolved. Therefore, the analysis is concluded by studying the numerical data at the end of this section. The other difference is that the faired skid-landing-gears significantly reduce the flow perturbations found in the wake of the baseline gear. In consequence the axial velocity fluctuations caused by the wake of the faired gears is barely discernible in Figs. 17 b) and c).

The following paragraphs conclude the analysis by cross-checking the results against the performed numerical simulations. Before the actual analysis is conducted, the numerical simulations are validated with experimental data.

Configuration	$C_{D,exp}$ [-]	$C_{D,sim}$ [-]	$C_{L,exp}$ [-]	$C_{L,sim}$ [-]
F0M0L0R0	0.302	0.311	0.046	0.065
F1M0L1	0.098	0.114	-0.104	-0.093
F1M0L2	0.093	0.099	-0.090	-0.055

Table 4. Comparison of experimental and numerical drag and lift coefficients (Re_∞ = 1.0 10^6, Ma_∞ = 0.116 , α = 0°, β = 0°).

Table 4 shows a comparison of numerical and experimental drag and lift coefficients for the numerically investigated configurations. These configurations are the baseline configuration including the skid-landing-gear and the rotor head and the fuselage with smoothed cabin bottom and faired landing-gear L1 and L2. In terms of drag the deviation between simulation and experiments ranges from 3 % up to 15%. However, only for configuration F1M0L1 the deviations between simulation and experiment exceed 10%.

The lift coefficients do not agree as well as the drag coefficients between simulation and experiments. The deviations from experiments are as large as 41%. The deviations for the lift coefficient are consistent in generally over predicting the produced lift though.

Fig.18. shows a comparison of experimental Stereo-PIV results and numerical results for contours of axial velocity deficit at one position near the rear fuselage upsweep of configurations F1M0L1 and F1M0L2. It can be seen that both through experiment and simulation a zone of negative axial velocity is detected. The extension of the recirculation zones is for both configurations approximately the same in the experimental and numerical data. However, its position is not reproduced precisely through the performed numerical simulations. This could explain the observed deviations discussed for the integral parameter. In particular, the large deviations for the lift coefficient could be related to this fact, since the rear fuselage upsweep is significantly contributing to the generation of lift. Please note that there are two artifacts in the experimental data for both configurations. One close to the end of the skid and one close to the central fuselage upsweep. Both are associated to obstructive light reflections at the model surface.

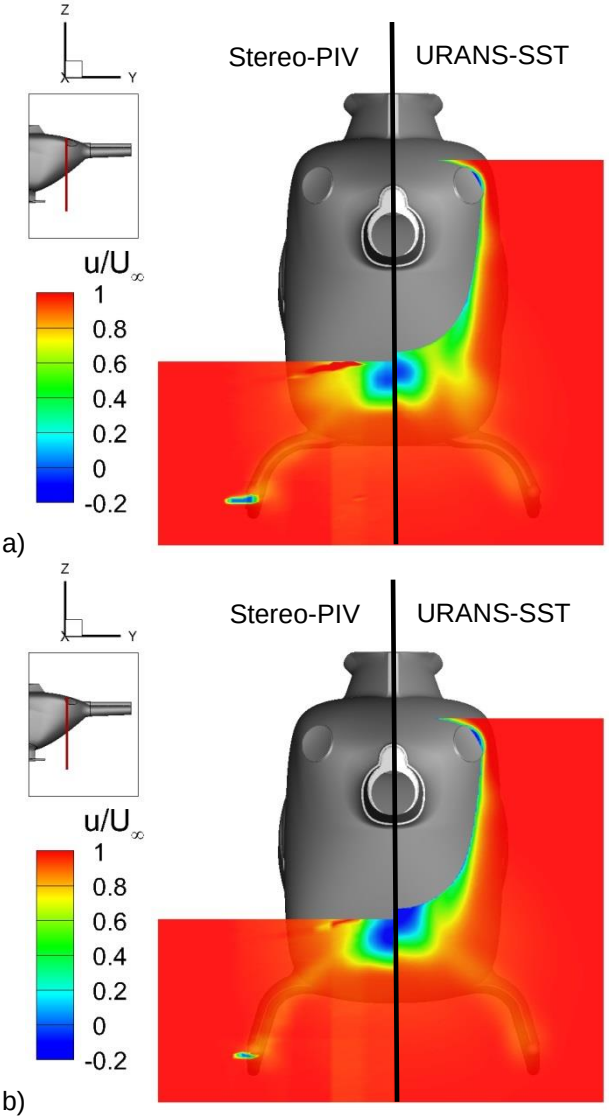

Fig. 18. Contours of velocity deficit near the rear fuselage upsweep of configurations a) F1M0L1 and b) F1M0L2 obtained both through experiment and simulation. Experimental values are averaged over all available Stereo-PIV data samples (about 100). The numerical results (URANS-SST) are depicted for one instance in time (Re_∞ = 1.0 10^6, Ma_∞ = 0.116 , α = 0°, β = 0°).

Fig. 19 shows contours of the surface pressure coefficient at the rear fuselage upsweep of configurations F0M0L0R0, F1M0L1 and F1M0L2 superimposed with near-surface streamlines. The results are showing one instance in time of the performed URANS-SST simulation for the stated configurations. Despite the discrepancies with the

experimental results some general characteristics become clear through this analysis.

In Fig. 19 a) the flow topology for the baseline configuration, including landing-gear and rotating rotor head, is depicted. It can be seen that the shear layer at the side of the fuselage is not rolling up into one concentrated upsweep vortex along each side. Such a strong vortex is not observed for the baseline configuration. Instead smaller vortices are formed along the separation line, indicated through the converging streamlines at the sides of the upsweep. However, on the aft-body of the configurations with the retrofittable and progressive faired-skid-landing-gear such a strong upsweep vortex is detected. This vortex is rolling up along almost the entire separation line. Hence, further evidence is found for the reasoning that the flow topology in the rear fuselage region is shifted from an eddy to a vortex type of flow. In the surface pressure contours in Fig. 19, the positive effect of the new faired landing-gear on interference drag can be identified. By attaching the faired landing-gear on the fuselage with smoothed cabin bottom the region of increased pressure on the rear fuselage upsweep is significantly enlarged, i.e. regions of yellow through red contour levels. Thus the region of separated flow is reduced. This also becomes clear from the near-surface streamline pattern. On the baseline configuration the recirculation zone basically spans over the entire region of the rear fuselage upsweep. With the faired landing-gears attached, the recirculation zone is confined to an outlined region at the lower central part of the fuselage upsweep.
There is a clear dependency of the separation region to the wake of the attaching elements. On the baseline configuration the blunt attaching elements lead to a fully detached flow at the attaching elements trailing edge. The velocity deficit caused in the wake then leads to a premature flow separation on the rear-fuselage and the appearance of the eddy-type of flow topology. However, with the retrofittable landing-gear L1 the separation at the attaching element is reduced. In consequence the velocity in the attaching elements wake increases which delays separation. Fig. 19 c) shows that the progressive design landing-gear L2 seems the most favorable design with respect to the landing-gear fuselage junction. The thin trailing edge of the L2 fairing effectively diminishes trailing edge separation. In consequence the separation at the rear fuselage upsweep is confined to its minimal extend of all configurations considered. This dependency of the separation at the rear fuselage upsweep of the separation at the junction between landing-gear and fuselage might also explain the difficulties in predicting the integral parameter precisely. In the performed simulation transition of the boundary layer is not considered through the fully turbulent representation of the equations. Thus separation and especially interdependent separation is difficult to predict.

Fig. 20 shows contours of axial vorticity in several planes downstream of the rear fuselage upsweep of configurations F0M0L0R0, F1M0L1 and F1M0L2 at one instance in time. For better comparability, the instance in time also shown in Fig. 19 is depicted.
Fig. 20 a) clearly shows the eddy-type of flow in the wake of the baseline configuration. Furthermore, the intense perturbation of the flow through the baseline skid-landing-gear becomes visible. The blunt components of the baseline gear shed a variety of small vortices into the wake, which then interact with the fuselage flow.

The structure of the wake downstream of the fuselage with smoothed cabin bottom and faired landing-gears deviates significantly from the eddy-state described before. For both configurations with faired landing-gears, see Fig. 20 b) and c) the pair of concentrated upsweep vortices on both sides of the fuselage are clearly discernible. Thus the shift to a vortex-type of flow through the attachment of the faired landing-gear becomes obvious.

Furthermore, the impact of the twist variation at the fairing of the outer cross-beams can be identified in the shown vorticity distribution. In consequence of the lift producing elements of the fairing a vortex-sheet is generated. In section 2 it is described that the twist-variation is defined such that the inner part of the cross-beam cover is set to positive incidence. It can be seen that a vortex sheet results from the circulation induced through the lift generated at exactly this section of the airfoil. Further downstream these vortex sheet roll up to another pair of counter-rotating vortices. These vortices then apparently also interact with the separation region on the rear fuselage upsweep as they are shed downstream.

6. Conclusions

In the framework of the CleanSky Joint Technology Initiative, the GRC subproject Aerodynamic Design Optimisation of a Helicopter Fuselage including a Rotating Rotor Head (ADHeRo) was initiated in order to increase the aerodynamic efficiency of light-weight rotorcraft. This paper reported on the ADHeRo skid-landing-gear optimisation campaign. It was conducted to confirm the drag reduction potentials for faired skid-landing-gears on a Twin Engine Light (TEL)-class utility helicopter. The skid-landing-gear optimisation campaign has provided valuable data both through wind tunnel experiments and numerical simulations. Based on the obtained data set, a detailed study of both global and local flow parameters has been performed.

The presented work also extended the analysis of the baseline configuration. Through the application of an internal strain gauge balance the skid-landing-gear and rotor head loads could be recorded separately.

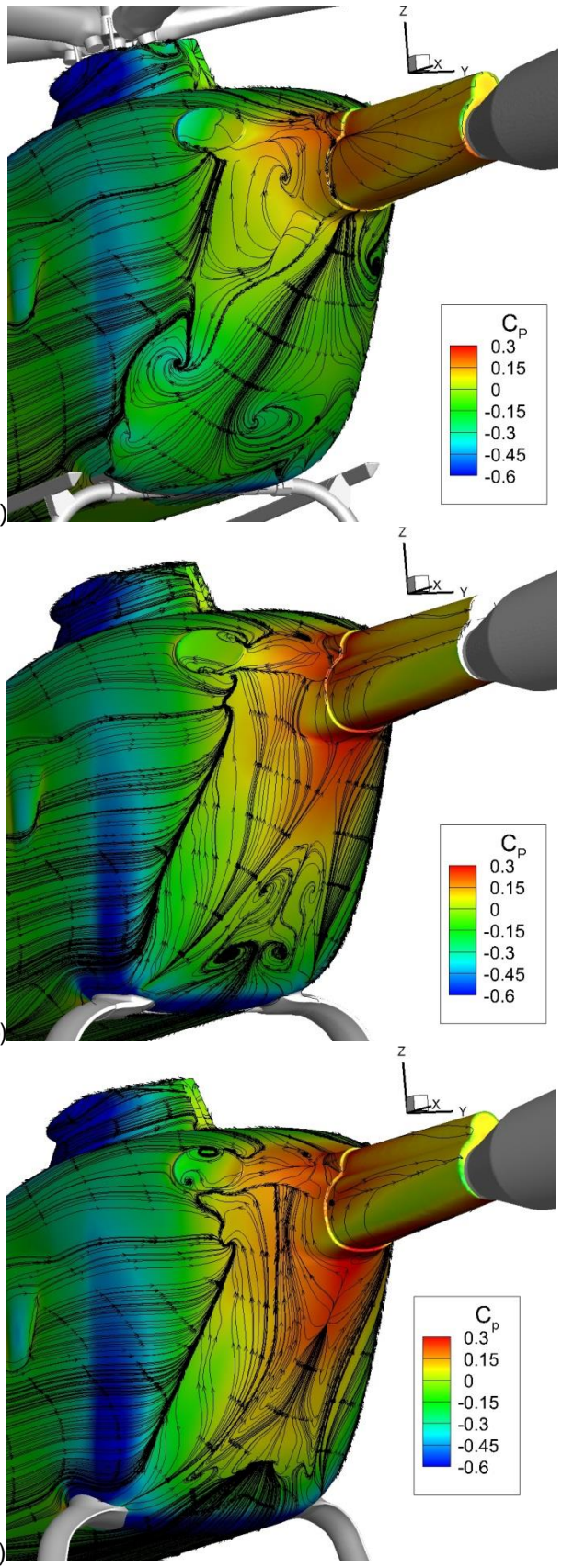

Fig. 19. Contours of pressure coefficient on the rear fuselage of configurations a) F0M0L0R0, b) F1M0L1, c) F1M0L2 - superimposed with near-surface streamlines at one instance in time, URANS-SST (Re_∞ = 1.0 10^6, Ma_∞ = 0.116 , α = 0°, β = 0°).

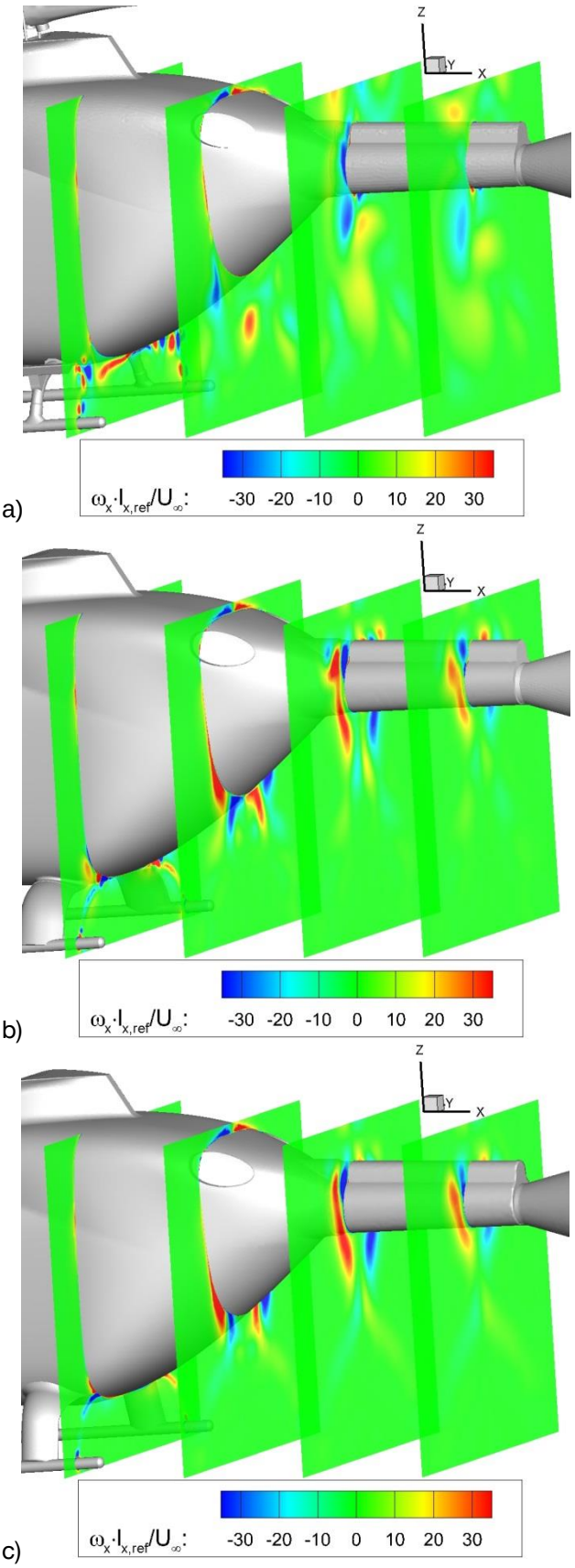

Fig. 20. Contours of non-dimensional axial vorticity in four planes, normal to the freestream direction, downstream of configurations a) F0M0L0R0, b) F1M0L1, c) F1M0L2 at one instance in time **(**Re_∞ = 1.0 10^6, Ma_∞ = 0.116 , α = 0°, β = 0°).

As a result, a full decomposition, including interference effects, of the baseline drag components is achieved. It was shown that for the baseline configuration the skid-landing-gear accounts for 30 % of the total parasite drag, whereof 3% are associated to interference drag on the fuselage.

Furthermore, it was revealed that a significant part of the parasite drag caused by the landing-gear can be obviated through the application of aerodynamic fairings. This study showed that fairing the cross-beams and the attaching elements of the landing-gear to the fuselage is essential for achieving efficiency gains. Two different fairings were considered, one retrofittable design L1 for current production helicopter and one progressive design L2 for next generation helicopter. Compared to the baseline model, which excludes the tail surfaces, the parasite drag is reduced by 24 % to 27% with the retrofittable and progressive landing-gear design, respectively. Smoothing the cabin bottom by removing attaching surfaces for additional equipment yields another 3 % drag benefit.
A negative impact of the faired skid-landings-gears was observed for their impact on lift. The configurations including the faired gears and rotor head generate down force instead of lift as observed for the baseline. With respect to the generated down force, the progressive design variant L2 performs significantly better than the retrofittable variant L1. The down force is cut in half when the landing-gear L2 is installed instead of L1. Thus overall the progressive design variant of the skid-landing-gear is the best variant for achieving efficiency gains.

However, future studies should also investigate the impact of the faired landing-gear on stability and control, e.g. pitching moment slope over angle of attack. Furthermore, the wake flow is shifted from an eddy- to a vortex-type when the faired skid-landing-gears are attached. This could lead to a changed incoming flow to the control surfaces at the tail. In consequence the static and dynamic stability of the fuselage could be affected. Hence the effectiveness of the control surfaces in the presence of the faired skid-landing gear should be revised.

Finally, further potential for optimising the fuselage drag and lift characteristics is identified. The analysis showed a strong sensitivity of the extension of the separation region on the fuselage upsweep to momentum losses at the fuselage bottom. Furthermore, in the presence of the faired landing-gears, strong upsweep vortices are detected. Therefore, it is expected that drag and down force at the fuselage can be further reduced through passive flow control measures at the rear fuselage. It is intended to achieve this through the application of vortex generators and strakes to reduce the adverse effect of the separation zone and the upsweep vortices, respectively.

Acknowledgments

The research leading to these results received funding from the European Community's Seventh Framework Program (FP/2007-2013) for the Clean Sky Joint Technology Initiative under grant agreement number 270563. The authors would like to thank project leader Eurocopter Deutschland GmbH for the fruitful collaboration and valuable support .Furthermore, special thanks are addressed to ANSYS CFX for providing the flow simulation software. The work of our students Philipp Brändle, Markus Spagl and Victor Stein is also highly appreciated.

REFERENCES

[1] Eurocopter Deutschland GmbH
[2] Grawunder, M. et al.: Flow Characteristics of a Helicopter Fuselage Configuration Including a Rotating Rotor Head. 28th International Congress of the Aeronautical Sciences, Brisbane (2012)
[3] Keys, C. N., Wiesner, R.: Guidelines for Reducing Helicopter Parasite Drag. Journal of the American Helicopter Society, Vol.20, Issue 31 (1975)
[4] M. Grawunder et al.: Flow Characteristics of a Five Bladed Rotor Head. Notes on Numerical Fluid Mechanics (2012).
[5] Menter, F R.: Zonal two-equation k-ω turbulence model for aerodynamic flows. AIAA Journal, Vol. 32, No. 8, pp. 1598-1605 (1994)
[6] ANSYS, Inc., CFX – Solver Theory Guide Release 14.5 (2012)
[7] Kneisch, T. et al.: Optimised rotor head design for an Economic Helicopter. Proceedings of the 37th European Rotorcraft Forum, Gallarate (2011)
[8] Reß, R. et. al.: Windkanaluntersuchung einer Hubschrauberzelle einschließlich eines rotierenden Rotorkopfes. 61. Deutscher Luft und Raumfahrt Kongress, Berlin (2012)
[9] Seddon, J., Newman S.: Basic Helicopter Aerodynamics. Second Edition, Blackwell Science, pp. 107 ff. (2002)

CLASSIFICATION & COPYRIGHT